

ATRP의 전자전달로 생성된 활성제를 이용한 산화그래핀의 표면기능화와 Poly(lactic acid)의 성능에 미치는 영향

Lang Zheng and Weijun Zhen[†] 

Key Laboratory of Oil and Gas Fine Chemicals, Ministry of Education and
Xinjiang Uygur Autonomous Region, Xinjiang University

(2017년 11월 14일 접수, 2018년 1월 24일 수정, 2018년 1월 30일 채택)

Surface Functionalization of Graphene Oxide via Activators Regenerated by Electron Transfer for Atom Transfer Radical Polymerization and Its Effect on the Performance of Poly(lactic acid)

Lang Zheng and Weijun Zhen[†] 

Key Laboratory of Oil and Gas Fine Chemicals, Ministry of Education and
Xinjiang Uygur Autonomous Region, Xinjiang University, Urumqi 830046

(Received November 14, 2017; Revised January 24, 2018; Accepted January 30, 2018)

Abstract: An improved Hummers method was used to prepare graphene oxide (GO). Then, the orthogonal experiment design methods were used to select the optimum conditions of preparation for graphene oxide-polymethyl methacrylate (GO-PMMA) via activators regenerated by electron transfer for atom transfer radical polymerization (AGET-ATRP). The optimum preparation conditions were determined by orthogonal tests. Furthermore, poly(lactic acid) (PLA)/GO-PMMA nanocomposites were prepared by melt blending to improve the comprehensive performance of PLA. Analysis results indicated that methyl methacrylate (MMA) was successfully grafted onto GO, and the addition of 0.3 wt% of GO-PMMA increased the tensile strength, elongation at break, and impact strength of PLA/GO-PMMA nanocomposites by 7.82, 40.66, and 50.62%, respectively, compared with PLA. Moreover, GO-PMMA eliminated the cold crystallization of PLA matrix and improved the crystallinity of PLA by 27.55%. In all, this study provided an effective and feasible method for improving the comprehensive performance of PLA.


Keywords: poly(lactic acid), graphene oxide, activators regenerated by electron transfer for atom transfer radical polymerization (AGET-ATRP), nanocomposites.

Introduction

Poly(lactic acid) (PLA) is a well-known green polymer material. Compared with traditional plastic, PLA has good biodegradability and biocompatibility.^{1,2} It is widely used in biomedical engineering,³ coating,⁴ film thermoplastic materials,⁵ textile⁶ and packaging⁷ engineering field.

In spite of these advantages, the low crystallinity, slow crystallization rate, poor impact resistance, poor heat resistance, and weak hydrophilicity of PLA has severely restricted its application in industry.⁸⁻¹¹ Therefore, it is necessary to modify

the PLA before the actual processing and application. Currently, the modified method can be simply divided into chemical and physical methods.¹² Among them, the physical method is to process a variety of materials or nano-filler and polylactic acid into composite materials. And the method does not need to carry on the chemical reaction, causing the modification process to be simplified, which is more suitable for the industrialization.¹³ In recent years, PLA has been modified with various nucleating agents such as montmorillonite,¹⁴ hydroxyapatite,¹⁵ carbon nanotubes¹⁶ and graphene.¹⁷ The addition of these nucleating agents can improve the performance of PLA to different degrees. However, at present, inorganic nucleating agents have been unable to meet the needs of industrial production, so the development of new organic nucleating agent is

[†]To whom correspondence should be addressed.
zhenweijun6900@163.com,  0000-0001-9225-489X
©2018 The Polymer Society of Korea. All rights reserved.

particularly important. The advantage is that organic nucleating agents have better compatibility with PLA. In addition, according to the molecular structure and nucleation factors of the nucleating agent and PLA, an organic nucleating agent with a specific functional group can be designed, which greatly improving the nucleation effect of the nucleating agent.¹⁸

Graphene oxide (GO) is an important derivative of graphene, which is obtained by chemical oxidation of natural graphite followed by ultrasonic stripping. Although the chemical oxidation process of GO destroys the highly conjugated structure of graphene, it retains the special surface properties and lamellar structure, and introduces a large number of oxygen-containing functional groups such as hydroxyl, carboxyl and epoxy groups.¹⁹ Functionalization based on these groups is a significant means to extend the scope of GO's application. Atom transfer radical polymerization (ATRP) is one of the most important and effective methods of reactive radical polymerization. It has the characteristics of fast reaction speed, mild reaction condition and wide range of available monomers.²⁰ And it is unmatched by other existing aggregation methods because of the excellent molecular design ability.

Activators regenerated by electron transfer for atom transfer radical polymerization (AGET-ATRP) is a method evolved from ATRP. As a new type of polymerization method, AGET-ATRP not only has all the advantages of traditional ATRP, and does not need to operate under anhydrous oxygen-free conditions, has been widely concerned.²¹ The results of the existing studies²²⁻²⁴ showed that ATRP method could give GO a variety of special functions, such as changing the surface polarity of GO to improve the dispersibility in solution and polymer, which could broaden the application of GO in various fields. Up to now, modified GO via the method of AGET-ATRP is very rare.

In this article, GO was first prepared by a modified Hummers method. Then, the methyl methacrylate (MMA) was grafted on the GO surface by AGET-ATRP method, and the optimum reaction conditions were determined by orthogonal experiment. Finally, PLA/GO-PMMA nanocomposites were prepared by melt blending. The structure and properties of the composites were studied.

Experimental

Materials. PLA (injection grade, $M_w=100000$ g mol⁻¹) was purchased from Shenzhen Guanghuaweiye Industrial Co. Ltd., Shenzhen, China. Flake graphite (average particle size 75 μ m)

was purchased from Qingdao Dahe Graphite Co., China. Concentrated H₂SO₄ was purchased from Kelong Chemical Reagent Factory, Chengdu, China. Potassium permanganate (KMnO₄) and concentrated hydrochloric acid (HCl) was purchased from Fuchen Chemical Reagent Factory, Tianjin, China. Hydrogen peroxide (H₂O₂, 30%) was purchased from Bodi Chemical Co., Ltd., Tianjin, China. Methyl methacrylate (MMA), ethyl 2-bromoisobutyrate (EBIB), triphenylphosphine (PPh₃) and ascorbic acid were purchased from Braunway Technology Co., Ltd., Beijing, China. *N,N*-dimethylformamide (DMF, >99%) and ferric chloride were obtained from Zhiyuan Chemical Reagent Co. Ltd., Tianjin, China. Methanol, sulfuric acid, and trichloromethane were all used without further purification.

Preparation of GO. GO was prepared according to the modified Hummers method.²⁵ Concentrated H₂SO₄ (150 mL) was taken in a 1000 mL three-necked flask and cooled in an ice-water bath. Then graphite (6 g) and NaNO₃ (3 g) were added under stirring. During the addition, the temperature was not allowed to rise above 10 °C. After stirring for some time, KMnO₄ (21 g) was slowly added over a period of 1 h and the reaction was further continued for 60 min. The reaction mixture was then heated to 35 °C and stirred for 120 min, till the solution turned purple to green. Then, deionized water (225 mL) was slowly added to the reaction mixture and heated to about 98 °C. The hydrolysis reaction was allowed to continue for 30 min. The temperature was lowered to 60 °C, followed by the slow addition of a certain amount of H₂O₂ (30%), till the reaction mixture turned golden yellow, and then filtered when hot. The filter cake was washed with 5% HCl and with deionized water until the filtrate was free of SO₄²⁻. The product was dialyzed for 7 days and freeze-dried to obtain graphite oxide.

Preparation of GO-PMMA Graft Copolymer. First, GO (0.1 g), methyl methacrylate (MMA, 5 mL), and DMF (20 mL) were ultrasonically dispersed in a 100 mL reaction flask for 30 min. Then FeCl₃·6H₂O (40 mg), triphenylphosphine (PPh₃, 80 mg), ethyl α -bromoisobutyrate (EBIB, 1 mL), and ascorbic acid (50 mg) were added into reaction flask. After 30 min of nitrogen was introduced, the reaction flask was sealed and placed in oil bath at 80 °C. After 8 h of magnetic stirring, the product was obtained. The product was dissolved in methanol (50 mL) and washed three times with trichloromethane to remove the self-aggregated product. Followed by filtration and drying in vacuum to obtain the GO-PMMA. The synthetic route of GO-PMMA is shown in Figure 1.

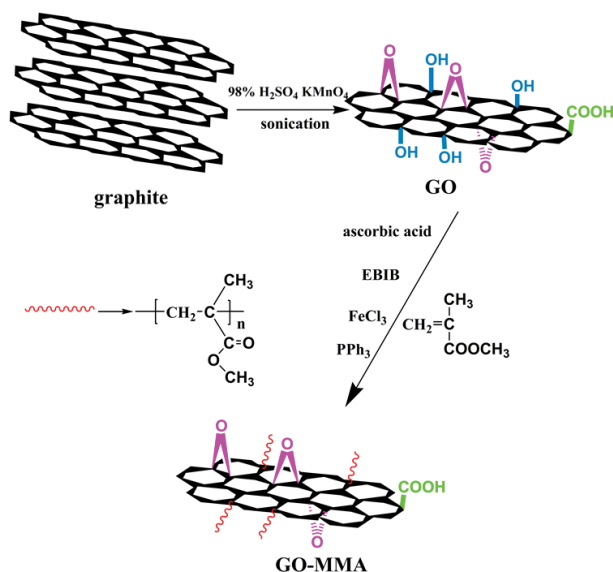


Figure 1. Synthetic route of GO-PMMA.

Preparation of PLA/GO-PMMA Nanocomposites. Poly (lactic acid) ($M_w=100000 \text{ g mol}^{-1}$) was dried for 24 h at 50 °C under vacuum to remove residual water. GO-PMMA was ultrasonically dispersed in acetone for 5 h. Acetone was then volatilized completely. Composites of PLA and GO-PMMA were prepared by manually feeding the mixture into a double-screw extruder (HAAKE Mini-Lab II, Karlsruhe, Germany, diameter=19 mm and L/D=25:1) at 180 °C, and the screw speed was held constant at 30 rpm. After these mixtures were extruded and pelletized, the PLA based nanocomposites were injection molded (HAAKE Mini Jet pro) into standard test specimens for tensile tests and impact tests. During injection molding, all samples were molded under 80 MPa pressure at 190 °C, mold temperature of 60 °C, and pressure-holding time of 10 s. In the PLA/GO-PMMA nanocomposites, the addition amounts of GO-PMMA were 0, 0.1, 0.2, 0.3, 0.4 and 0.5 wt%, respectively. Accordingly, PLA/GO-PMMA nanocomposites were named PLA0, PLA1, PLA2, PLA3, PLA4 and PLA5, respectively.

Characterization. Fourier transform infrared spectroscopy (FTIR) of the samples as carried out on a Bruker Equinox 55 (Karlsruhe, Germany) spectrometer using standard KBr pellet/disk technique. Spectra were recorded over a spectral range of 4000 to 400 cm^{-1} with a resolution of 4 cm^{-1} .

The chemical compositions of graphite, GO, and GO-PMMA were determined by X-ray photoelectron spectrometer (XPS). XPS (ESCALAB 250Xi, Thermo Fisher Scientific, USA) using a monochromatic Al K α X-ray source (1486.6 eV)

was used for the analysis. The off-axis charge neutralization gun was used to neutralize the positive charge on the samples surface. The pass energy 50 eV (full spectrum) and 30 eV (narrow spectrum) were used for the survey spectra. All binding energies were referenced to the C1s hydrocarbon peak at 284.5 eV.

X-ray diffraction (XRD) patterns were obtained using a Philips X'Pert X-ray diffractometer (Almelo, the Netherlands) with CuK α X-ray source at $\lambda=0.1540 \text{ nm}$ (50 kV, 35 mA). Diffraction spectra were obtained over a 2θ range of 5–40° with a scanning speed of 0.1° sec^{-1} .

Transmission electron microscope (TEM, TECNAI G2-F20 FEI Co., the Netherlands) was used to detect the morphology of GO, GO-PMMA and PLA/GO-PMMA nanocomposites. Specimen was observed at an acceleration voltage of 75 kV.

Scanning electron microscopy (SEM) (Inspect F, FEI Instrument Co., Ltd., Eindhoven, the Netherlands) at 20 kV of accelerating voltage was employed to study the impact fracture morphology. Prior to SEM analysis, the samples were sputter coated with gold to prevent charging during the tests.

Thermogravimetric analysis was conducted on an SDT-Q600 thermogravimetric analyzer (TA Instruments, New Castle, DE, USA). Each sample (about 5–10 mg) was heated at a heating rate of 10 °C min^{-1} in the temperature range of room temperature to 500 °C under nitrogen flow (100 mL min^{-1}).

Differential scanning calorimetry (DSC) of each sample (about 5–8 mg) was conducted on a DSC Q2000 differential scanning calorimeter (TA Instruments, New Castle, DE, USA). All test carried out under nitrogen flow (50 mL min^{-1}). The samples were heated from room temperature to 180 °C at a rate of 10 °C min^{-1} and held at a constant temperature for 3 min to eliminate the thermal history. The samples were then cooled to 25 °C at a rate of 5 °C min^{-1} (liquid nitrogen) and the temperature was maintained for 3 min. Finally, the temperature was raised to 180 °C at a rate of 10 °C min^{-1} , and the DSC curve of the process was recorded. The peak and enthalpy values were calculated by TA universal analysis.

The spherulitic morphologies of the samples were investigated by polarized optical microscopy (POM) (CSS450, Linkam Scientific, Tadworth, England). The samples were heated to 200 °C at a rate of 50 °C min^{-1} and held at a constant temperature for 3 min to eliminate the thermal history. And then the samples were cooled to 130 °C at 50 °C min^{-1} for isothermal crystallization. The spherulites micrographs of PLA and PLA nanocomposites were studied during isothermal crystallization.

Tensile tests were carried out according to ASTM D638 using instron 4302 universal testing machine (USA) at a cross-head speed of 5 mm min⁻¹. At least five measurements for every sample were made. Samples of PLA nanocomposites were standard test specimens from the injection mold.

Notched izod impact testing was carried out using a Testing Machines Inc. (TMI) 43-02-01 monitor/impact machine (New Castle, DE, USA) according to ASTM D256. Two-millimeter-deep notches were cut into sample beams using a TMI notch cutter. All results presented were the average values of five measurements.

The rheological behaviors of all samples were studied using a stress-controlled rotational rheometer (AR2000ex, TA Instruments, USA) with 25 mm diameter and 1 mm gap parallel plates. Before the measurement, each disk-shaped specimen, prepared by compression molding, was heated to 170 °C and held for 3 min to completely melt PLA and the nucleating agents. Deformation in the linear viscoelastic region was found to be 2%, and this was chosen for all subsequent frequency sweep tests. Samples were equilibrated at 170 °C before testing. The frequency was varied from 0.1 to 100 rad sec⁻¹.

The capillary rheological analysis of the samples was investigated by trace a mixed rheometer (MiniLab II, HAAKE, Germany). The samples of 7 g were melted at 180 °C for 0.5 min and then were sheared from 1 to 50 rpm at 180 °C.

Results and Discussion

Design of Orthogonal Experiments. For optimizing the preparation of GO-PMMA graft copolymer, the grafting rate was used as the objective function. The reaction time (A), the ratio of FeCl₃·6H₂O/triphenylphosphine (PPh₃)/EBIB (mg:mg:mL) (B), the quality of ascorbic acid (C), and reaction temperature (D) were selected as the four effect factors as the object of the orthogonal experiment. By the orthogonal design experiment of L₉ (3⁴) (Table 1),²⁶ optimum conditions were selected, and the grafting rate was evaluated on the basis of the optimum conditions. The samples obtained in experiment 1 to experiment 9 were named Sample 1 to Sample 9, respectively. Moreover, thermogravimetric analysis (TGA) was used to estimate the grafted MMA content on GO (Figure 2). The analytic results were presented in Table 2, in which the impact factor of each level for AGET-ATRP modification was found to be 6.060, 17.797, 21.647, and 21.576, respectively. According to the results, the C factor (the quality of ascorbic acid) had the greatest influence on the modification of GO, and the other

Table 1. Results Obtained from the Orthogonal Experiment of Preparation of GO-PMMA

Numbers	Factors				Grafting rate (%)
	A	B/	C	D	
1	1	1	1	1	12.24
2	1	2	2	2	42.73
3	1	3	3	3	44.47
4	2	1	2	3	44.91
5	2	2	3	1	15.97
6	2	3	1	2	39.04
7	3	1	3	2	56.18
8	3	2	1	3	16.43
9	3	3	2	1	45.01
K ₁ ^a	33.147	37.777	22.570	24.407	
K ₂	33.307	25.043	44.217	45.983	
K ₃	39.207	42.840	38.873	35.270	
R ^b	6.060	17.797	21.647	21.576	

Effects of factors on experimental results: C > D > B > A; Optimum conditions: C₂D₂B₃A₃

^aK_i denotes the arithmetic mean of the experimental results obtained by taking the factor on the ith column. ^bR is the difference between the maximum and minimum values in either column.

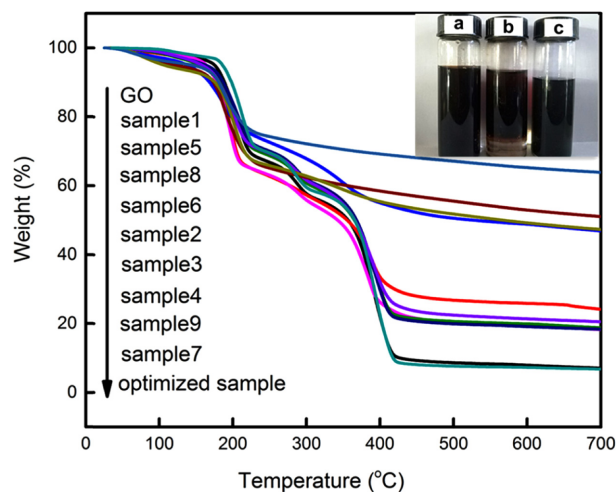


Figure 2. Thermogravimetric curve of the samples and dispersion of GO and GO-PMMA in solvent: (a, b) GO dispersed in water and trichloromethane, respectively; (c) GO-PMMA dispersed in trichloromethane.

factors, which also had influence on modification of GO, were as follows: reaction temperature, reaction ratio, and reaction time. The results of the orthogonal analysis showed the optimum reaction conditions to be a reaction temperature of 80 °C,

reaction time of 9 h, ascorbic acid quality of 50 mg, and $\text{FeCl}_3 \cdot 6\text{H}_2\text{O}:\text{PPh}_3:\text{EBIB}$ of 50:90:1.5 (mg:mg:mL). The grafting rate of GO-PMMA prepared under this condition was 56.48%.

The monomer conversion under the optimum condition was checked by weighing method. The samples were taken out at regular time and a drop of hydroquinone solution was added, followed by drying at 120 °C oven for 1 h, and the dry weights were obtained. The monomer conversions were calculated from the percentages of dry weight divided by monomer feed.^{27,28} Figure 3 illustrates the total monomer conversion of MMA varied over time. In Figure 3, the monomer conversion of MMA increased continually with reaction time. The curve was gradually stabilized after 500 min, and the monomer conversion reached 58.22% at the end of the reaction.

As can be clearly seen from Figure 2, the GO weight loss was between 150 to 250 °C, which results from the decomposition of labile oxygen functional-containing groups. While the weight loss of Sample 1 to Sample 9 were mainly between 150-250 °C and 300-440 °C, which was due to MMA mono-

mer introduced methyl groups and other groups.²⁹ In addition, GO and GO-PMMA were placed in a solution of 1 mg / mL, and after 7 days, the digital photographs were shown in Figure 2. It can be seen from Figure 2(a), GO had a good dispersion and no precipitation, indicating good hydrophilicity, so it could be stable in the water long-term dispersion. Figure 2(b) showed that GO was still dispersed in water and did not transfer to trichloromethane, indicating that GO will not be dispersed in trichloromethane. In Figure 2(c), GO-PMMA was still stable in trichloromethane, proving that MMA was successfully grafted onto GO, which greatly improved its lipophilicity.³⁰

FTIR Analysis. From the results of FTIR spectra, one can speculate the probable interactions between the PMMA and the GO. Figure 4 shows the FTIR spectra of PMMA, GO, and GO-PMMA. It could be seen that GO contained a large number of hydrophilic groups. The peak at 3425 cm^{-1} was due to the asymmetric stretching vibration of the hydroxyl group (-OH). The peak at 1728 cm^{-1} could be attributed to the stretching vibration of the carbonyl group (C=O), whereas the peak at 1627 cm^{-1} resulted from the stretching vibrations of the unoxidized carbon-carbon double bonds (C=C). The peak at 1220 cm^{-1} was ascribed to the symmetrical stretching vibration of the carbon-oxygen bonds (C-O) of the epoxy group and the peak at 1061 cm^{-1} was the absorption peak of C-O. After functionalization with the PMMA, the spectrum of the GO-PMMA was similar to that of the PMMA. The new peaks at 2997 cm^{-1} and 2950 cm^{-1} were C-H stretching vibration peaks.³¹ And the cluttered and dense peaks appeared at 500 to 1600 cm^{-1} , which

Table 2. Factor Level of the Orthogonal Experiment $L_9(3^4)$ of Preparation of GO-PMMA

Level	Factors			
	A/Reaction time (h)	B/ $\text{FeCl}_3 \cdot 6\text{H}_2\text{O}/\text{PPh}_3/\text{EBIB}$ (mg:mg:mL)	C/Vc (mg)	D/Reaction temperature (°C)
1	7	30/60/0.5	30	70
2	8	40/80/1	40	80
3	9	50/90/1.5	50	90

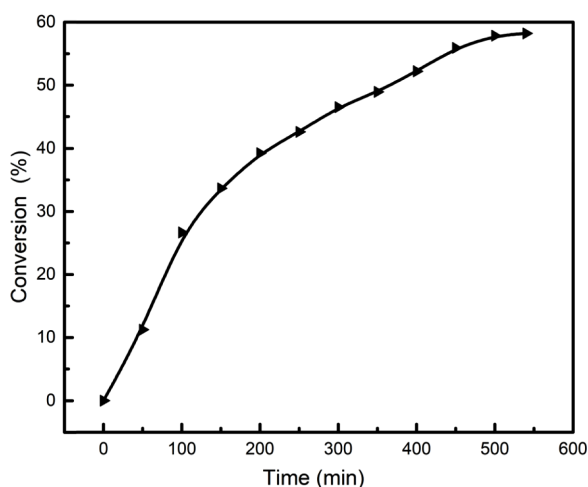


Figure 3. Relationship between MMA conversion and reaction time.

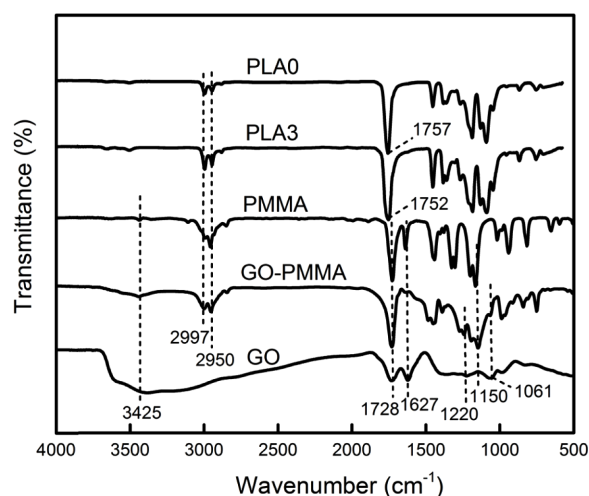


Figure 4. Fourier transform infrared spectra of GO, GO-PMMA, PMMA, PLA0 and PLA3.

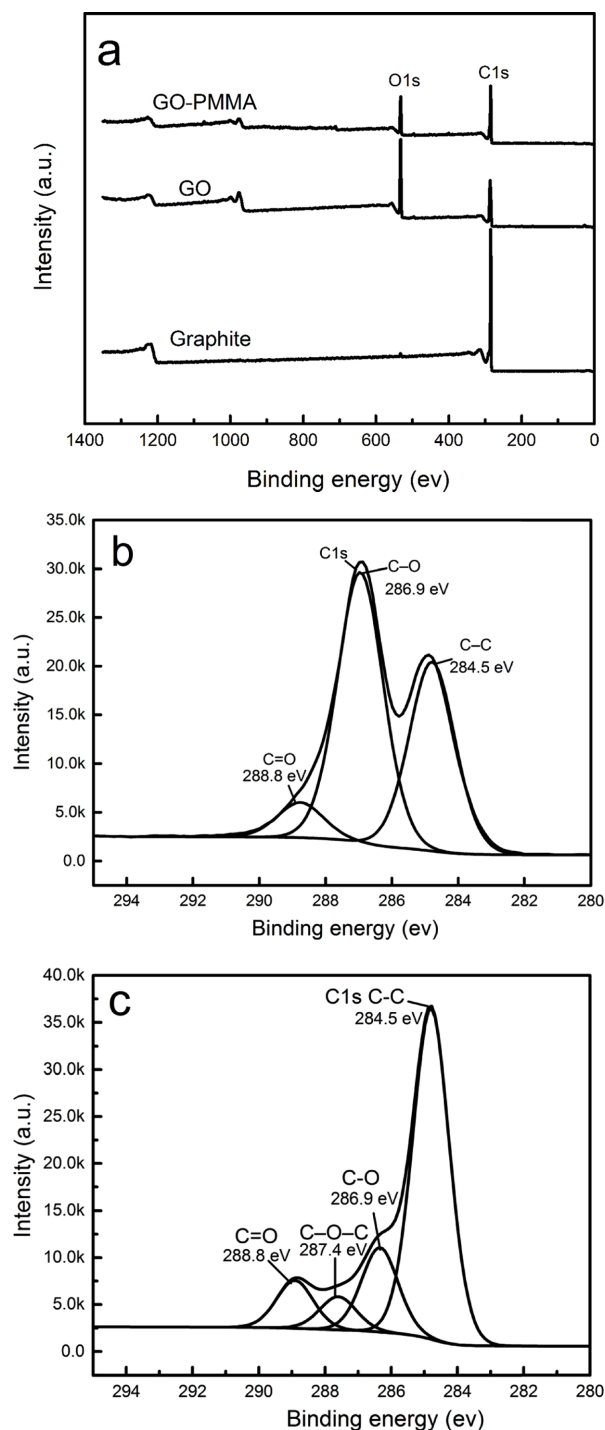


Figure 5. XPS analysis of graphite, GO and GO-PMMA: (a) full spectrum of graphite, GO and GO-PMMA; (b) C spectrum of GO; (c) C spectrum of GO-PMMA.

was similar to PMMA. FTIR analysis showed that the PMMA group was successfully introduced into GO after AGET-ATRP reaction. Furthermore, FTIR analysis of PLA0 and PLA3 are

Table 3. XPS C1s Peak Position and the Relative Atomic Percentage in Different Functional Groups of Graphite, GO, and GO-PMMA

Sample	C1s contribution/% (the relative atomic percentage)		
	C-C	C-O	C=O
Graphite	88.42	10.34	1.06
GO	36.28	52.86	10.86
GO-PMMA	59.78	18.01	22.21

shown in Figure 4. The absorption peak at 1757 cm^{-1} was the C=O characteristic absorption peak of pure PLA. Due to the addition of the nucleating agent GO-PMMA, the C=O characteristic absorption peak was shifted to a low wavenumber of 1752 cm^{-1} . This could be explained by the fact that the C=O in the PLA and the O-H in the GO-PMMA formed hydrogen bonds,³² resulting in the charge being separated from the C=O bonds to the other atoms. The double bond property of C=O was reduced and the absorption frequency decreased, which led to the characteristic peak of C=O shifted toward a low wavenumber.

XPS Analysis. XPS offers direct evidence for the elemental composition of graphite, GO, and GO-PMMA. The XPS spectra and analysis of graphite, GO and GO-PMMA are shown in Figure 5 and Table 3. The C/O atomic ratio (60.04%/39.49%) of GO confirmed the successful oxidation of graphite. The C1s peaks in the XPS spectra of graphite, GO, and GO-PMMA were split into four peaks, which could be attributed to carbon atoms with different functional groups, including the non-oxygenated ring carbon (284.5 eV), C-O-C (287.4 eV), C=O (288.8 eV), and C-O (286.9 eV) bonds. It can be seen from Figure 5 that a large amount of C=O and C-C are introduced into the GO during grafting process. In addition, the results of Table 3 showed that the C-C content of GO-PMMA increased from 36.28% to 59.78%, and the content of C=O increased from 10.86% to 22.21%.³³ This proved that the MMA monomer was successfully grafted onto GO by AGET-ATRP reaction.

XRD Analysis. Figure 6 shows the XRD patterns of graphite, GO, GO-PMMA, PLA, and PLA3. The Bragg's equation can be used to calculate the slice spacing of graphite and its derivatives. The equation is as follows: $2d\sin\theta = n\lambda$, $n = 1$. The diffraction peak of graphite appeared at about $2\theta = 26.5^\circ$ and the interlayer spacing was 0.336 nm. The diffraction peak was sharp with high peak intensity, which indicated that the graphite crystal was regular, and the crystallinity and degree of orientation were high. The intensity of the diffraction peak of GO was significantly reduced and the interlayer distance was

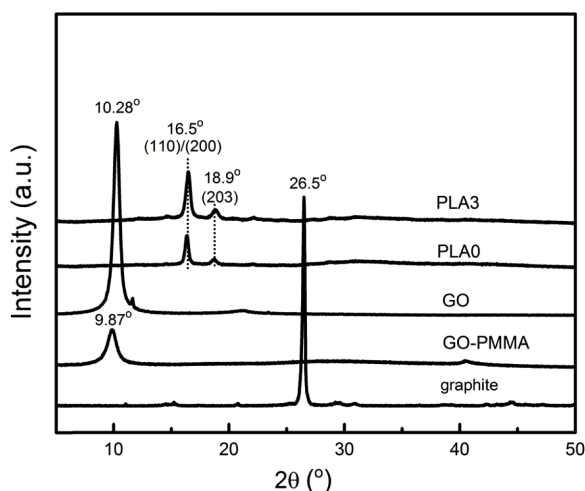


Figure 6. X-ray diffraction spectra of graphite, GO, GO-PMMA, PLA0, and PLA3.

0.859 nm, which suggested that after the introduction of a large number of polar groups such as oxygen-containing functional groups, the interlayer spacing was significantly increased and the crystal structure was destroyed. The diffraction peak for GO-PMMA appeared at $2\theta = 9.87^\circ$, which was due to the introduction of the methyl, carbonyl and other functional groups, and the interlayer distance was further increased to 0.895 nm. This result was in accordance with that reported by other researchers.³⁴ For PLA0, two sharp characteristic diffraction peaks are shown at 16.5° and 18.9° , corresponding to (110)/(200) and (203) planes, respectively. This indicated that the lattice structure of PLA exhibited an alpha crystal shape. For the PLA3, the similar diffraction patterns were observed, indicating that the incorporation of GO-PMMA didn't modify the crystal structure of PLA in the nanocomposites. However, the peak intensity of PLA3 diffraction peak was greater than

PLA0, which indicated that the addition of GO-PMMA could effectively promote the crystallization of PLA. In Figure 6, the reflection of graphite oxide was present at around $2\theta = 10.28^\circ$, while it was absent in the PLA3, suggesting that the layered GO-PMMA had been exfoliated in the nanocomposites. H. Wang,³⁵ etc., also made a similar report. In all, the crystal structure of PLA remains unchanged despite the addition of GO-PMMA in the nanocomposites.

TEM Analysis. For a detailed morphology, TEM analysis of GO and GO-PMMA was performed by placing drops of the dispersions directly on the carbon-coated microgrids. As can be seen from Figure 7(a), the surface and the edge of the GO sheet were crimped and wrinkled, and the lamellae were relatively loose and thinner. This was due to the role of strong oxidants, the graphite layer was inserted into some oxygen-containing functional groups, and then under the action of ultrasound peeling. In addition, the sheet surface of GO had a large specific surface area. In order to reduce its surface energy and maintain the stability of the two-dimensional crystal structure, the surface and the edge of the graphene were easily bent and wrinkled. Figure 7(b) depicts the GO-PMMA sample with polymer dark features on the surface of GO nanosheets. Comparing Figure 7(a) and 7(b), we can identify the smooth surface of GO (Figure 7(a)) and continuous PMMA films on the graphene.³⁶ To reveal the dispersibility of GO-PMMA in PLA matrix, PLA3 was investigated with TEM in this work. As shown in Figure 7(c), no significant particulate material was found. In contrast, it was found that the flexible and wrinkled sheets of GO were well dispersed in the PLA matrix, indicating that GO-PMMA had been primarily stripped and randomly dispersed at the molecular level.³⁷

Mechanical Properties. The effects of GO-PMMA on the mechanical properties of pure PLA are shown in Figure 8. It

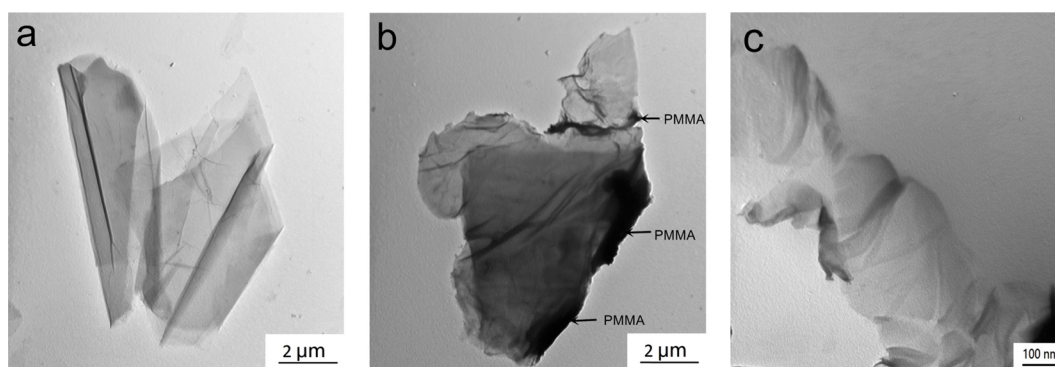


Figure 7. TEM images of GO, GO-PMMA and PLA/GO-PMMA nanocomposites: (a) GO; (b) GO-PMMA; (c) PLA3.

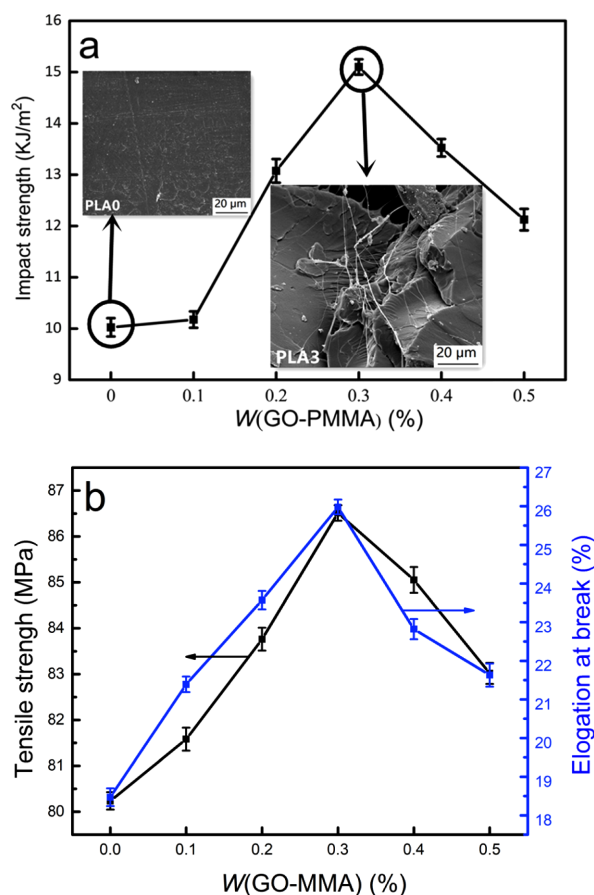


Figure 8. Effects of GO-PMMA on mechanical properties of PLA/GO-PMMA nanocomposites: (a) impact strength; (b) tensile strength and elongation at break.

could be seen from the Figure 8 that the addition of GO-PMMA significantly improved the mechanical properties of the PLA. With an addition of GO-PMMA increased by 0.3%, the mechanical properties of PLA nanocomposites reached the maximum values. The tensile strength, elongation at break, and impact strength of the PLA nanocomposites were increased by 7.82, 40.66, and 50.62%, respectively, compared with PLA. The mechanical properties of PLA nanocomposites gradually decreased with further increase in the amount of GO-PMMA. This could be explained by the fact that a small amount of GO-PMMA could be uniformly dispersed in the PLA matrix, many nano-lamellars were well embedded in the PLA matrix, so that the two components had a strong interface between the interaction. This limited the movement of polymer chains near the surface of GO-PMMA, thereby enhancing the mechanical properties of nanocomposites.³⁸ Simultaneously, GO-PMMA played the role of heterogeneous nucleation in PLA matrix. This made the crystallization process to form the

smaller spherical crystal size. When the nanocomposites were plastically deformed by external forces, a large number of small-sized grains resulted in less stress concentration, which showed the improvement of mechanical properties.³⁹ With increase in GO-PMMA addition, GO-PMMA lamellae were agglomerated, which reduced the physical crosslinking at the nanoscale. And the combination of GO-PMMA and PLA interface was poor, which led to a weak contact between the two. When subjected to external forces, the stress concentrated at these locations, the material will break down prematurely, resulting in reduced mechanical properties of the nanocomposites.⁴⁰

Fracture SEM Analysis. The fracture characteristics of PLA and PLA3 were studied by SEM, which confirmed the effects of addition of GO-PMMA on the mechanical properties of the materials. It was evident from Figure 8(a) that a section of neat PLA (PLA0) was relatively flat. Since there was no obvious yield phenomenon, it showed brittle fracture. However, in Figure 8(a) (PLA3), the GO layer was coated with PLA matrix, which was dispersed in the PLA matrix in a disorderly manner. A large number of dimples and oriented fibers appeared, which clearly showed characteristics of toughness fracture. This kind of structure could absorb more impact energy when the composite was impacted, which showed the increase of toughness of the material.⁴¹ These results indicated that GO-PMMA had a very good plasticizing effect on PLA nanocomposites, which changed the characteristics from brittle fracture to ductile fracture. The addition of GO-PMMA helped improve the performance of PLA, which was consistent with the results from the analysis of mechanical properties.

Thermogravimetric Analysis. The thermal stability of PLA and PLA3 was evaluated by TGA, as shown in Figure 9. The temperatures for 5% (T_5) or 50% (T_{50}) weight loss and the initiation (T_{onset}), maximum (T_{max}), and final decomposition (T_{end}) of PLA0 and PLA3 could be extracted from the TGA curves and the results were summarized in Figure 9. The values for T_{onset} and T_{max} of PLA3 were higher than those of pure PLA. Clearly, after adding GO-PMMA, the T_5 , T_{50} , T_{onset} , T_{max} , and T_{end} values increased significantly. In particular, T_{end} and T_5 of PLA increased more than 10 °C, owing to the introduction of GO-PMMA. This indicated that the thermal stability of the PLA3 was greatly improved compared with that of neat PLA. This could be explained in two ways, on one hand, oxygen-containing functional groups and surface chemical defects on the GO-PMMA layer could form hydrogen bonds with oxygen-containing functional groups on the PLA molecular

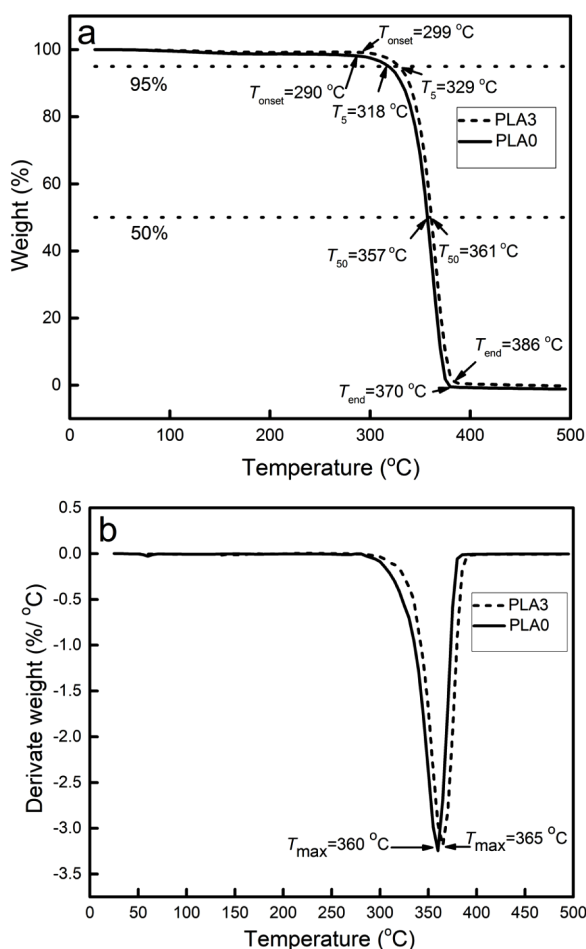


Figure 9. Thermogravimetric curves for PLA0 and PLA3: (a) thermogravimetric curves for PLA0 and PLA3; (b) differential thermogravimetric curves for pure PLA0 and PLA3.

chains, which enhanced the binding force between the GO-PMMA and PLA.⁴² On the other hand, the GO-PMMA could form a spatial reticular structure in the PLA matrix, which restricted the activity of the PLA molecule chains. And the carbon monoxide, carbon dioxide and other gases produced in the process of thermal decomposition were difficult to escape, which effectively inhibited the thermal decomposition rate of nanocomposites.⁴³

Differential Scanning Calorimetric Analysis. Differential scanning calorimetry (DSC) is a technique for measuring the heat flow rate of a sample relative to a reference material with temperature changes under the control of a temperature program. It is often used to determine the melting heat, crystallinity and glass transition temperature of the polymer, which has become one of the indispensable means to characterize the properties of polymers. Figure 10 shows the DSC curves of

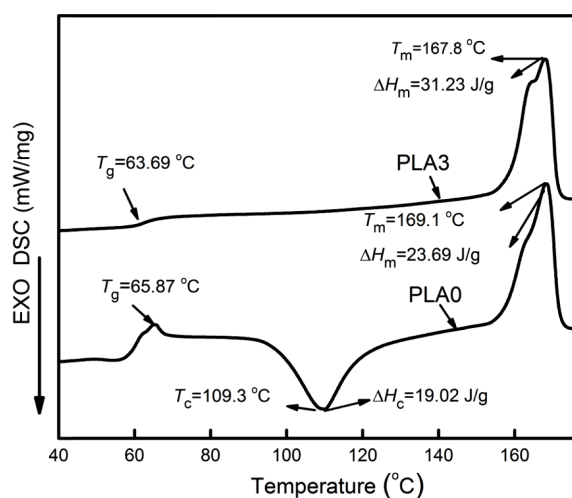


Figure 10. Differential scanning calorimetry curves of PLA0 and PLA3.

PLA0 and PLA3. The thermal properties of PLA0 and PLA3 are summarized in Figure 10. The degree of crystallinity (X_c) was determined from DSC analysis data using eq. (1), where ΔH_m , ΔH_c , and f were the measured melting enthalpy, cold-crystallization enthalpy, and weight fraction of PLA, respectively. In Figure 10, T_m and T_c were the measured melting temperature and cold-crystallization temperature, respectively. The crystallinity of the polymer was calculated from the equation, where was the melting enthalpy expected for a polymer with 100% crystallinity, and the heat of fusion ΔH_m^0 of pure PLA was 93.7 J g^{-1} .⁴⁴

$$X_c = (\Delta H_m - \Delta H_c) \div (f \times \Delta H_m^0) \times 100\% \quad (1)$$

It could be seen from the Figure 10 that the cold crystallization peak of PLA3 (0.3% GO-PMMA content) disappeared. This was due to the addition of GO-PMMA reduced the activation energy of PLA lattice, which promoted the crystallization of PLA and effectively suppressed the cold crystallization of PLA matrix.⁴⁵ Figure 10 showed that the T_m of PLA0 was 169.1°C , whereas the T_m of PLA3 decreased to 167.8°C , which suggested that GO-PMMA could form hydrogen bonds with PLA, since GO-PMMA played the role of a heterogeneous nucleating agent.⁴⁶ Moreover, the X_c of PLA3 was 32.20%, compared with PLA0 with an X_c of 4.65%, which also demonstrated that GO-PMMA improved the crystallinity of PLA. This was the result of heterogeneous nucleation effects brought about by the nucleating agents that improved the crystallization of PLA.

Polarized Optical Microscopic Analysis. For a crystalline polymer, the crystallization rate of PLA is very crucial for practical processing applications. The crystallization process of a polymer mainly includes nucleation and grain growth. Therefore, the crystallization rate mainly includes nucleation rate, crystal growth rate, and total crystallization rate. The number of nuclei and the rate of spherulite formation of PLA were observed under a polarizing microscope to study the nucleation rate and crystal growth rate of the polymer. Figure 11 shows the POM results of the isothermal crystallization process of pure PLA and PLA3 at 130 °C, from which the effect of GO-PMMA addition on nucleation rate and nucleation density of PLA could be studied. It could be seen from the diagram that all the spherics showed a typical black extinction structure. It was obvious that the spherulite number of PLA3 was much larger than that of PLA0 at the same crystallization time. This could be explained by the fact that the nanostructure of GO-PMMA as nucleating agent, which was homogeneously dispersed in the PLA matrix. As a result, the nucleation density of PLA was greatly improved. In addition, Figure 12 shows the spherulite radius of PLA0 and PLA3, which change with time during the isothermal crystallization at 130 °C.⁴⁷ It is observed from the Figure 12 that the spherulite radius of PLA0 and PLA3 increases linearly with time. Therefore, the growth rate G of spherulites could be obtained from the slope of the two straight lines in the graph. By fitting, the spherulite growth

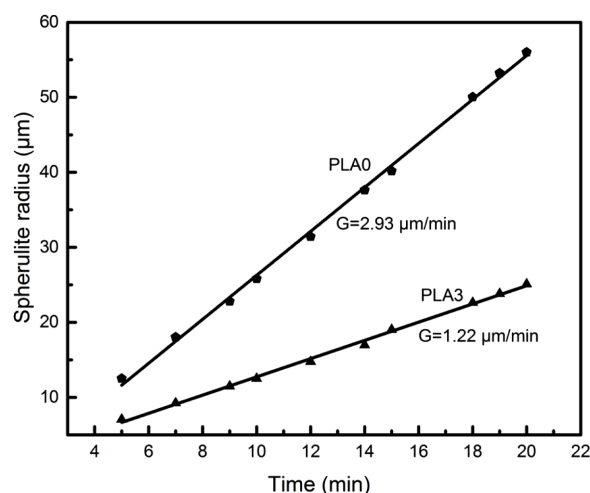


Figure 12. Changes of spherulite radius as functions of time PLA0 and PLA3 during isothermal crystallization at 130 °C.

rates of PLA0 and PLA3 were 2.93 and 1.22 μm/min, respectively. It could be explained that the number of spherulites in the same area increases with the addition of nucleating agent GO-PMMA, spherulites collided with each other, which greatly limited the growth of spherulites.⁴⁸ In summary, the total crystallization rate of PLA3 was much larger than that of PLA0. POM analysis further confirmed that GO-PMMA induced the crystallization of PLA more efficiently, which was in accordance with the aforementioned DSC results.

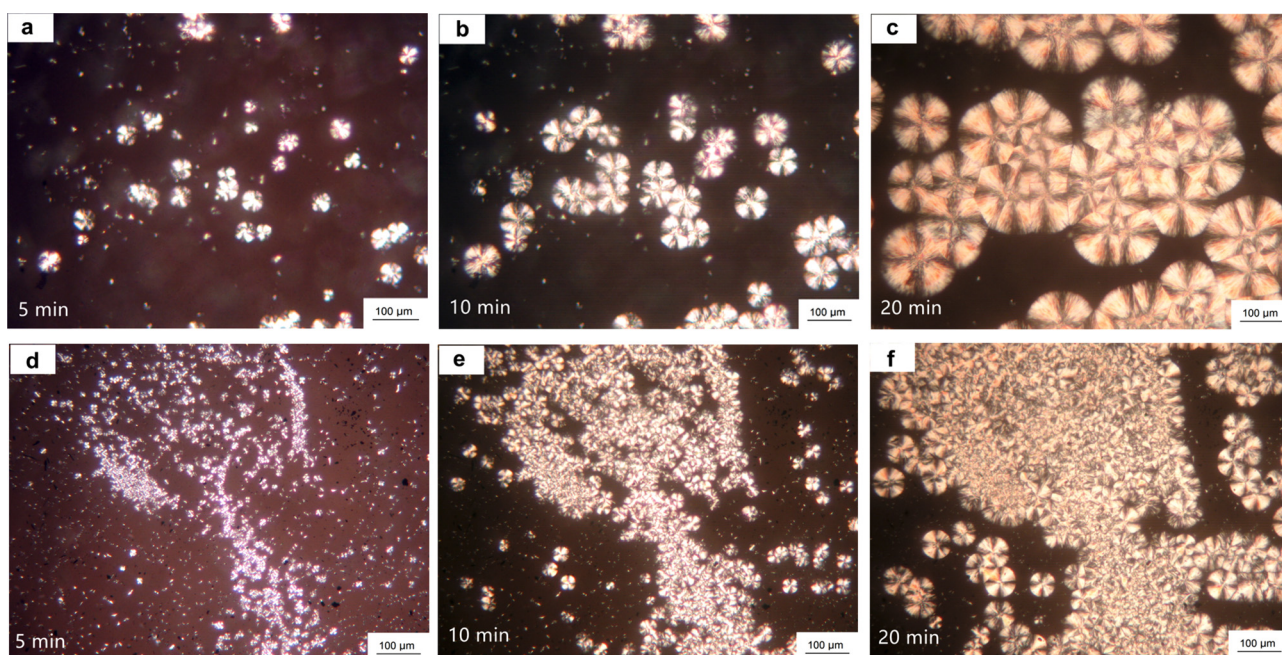


Figure 11. Selected POM micrographs taken during isothermal crystallization at 130 °C for PLA0 (a, b, c) and PLA3 (d, e, f).

Rheological Behavior Analysis. The storage modulus characterized the energy stored in the deformation process due to elastic deformation. This was proportional to the maximum elasticity stored in each cycle of the material, reflecting the elasticity of the viscoelastic material. The more the storage modulus, the higher is the rigidity of the material, and the less

difficult is it for the material to deform. The loss modulus is the amount of energy lost due to viscous deformation (irreversible) when the material is deformed. It mainly reflects the viscosity of the material, which is used to characterize the material loss factor.

Figure 13(a) and Figure 13(b) are the diagrams of PLA0 to

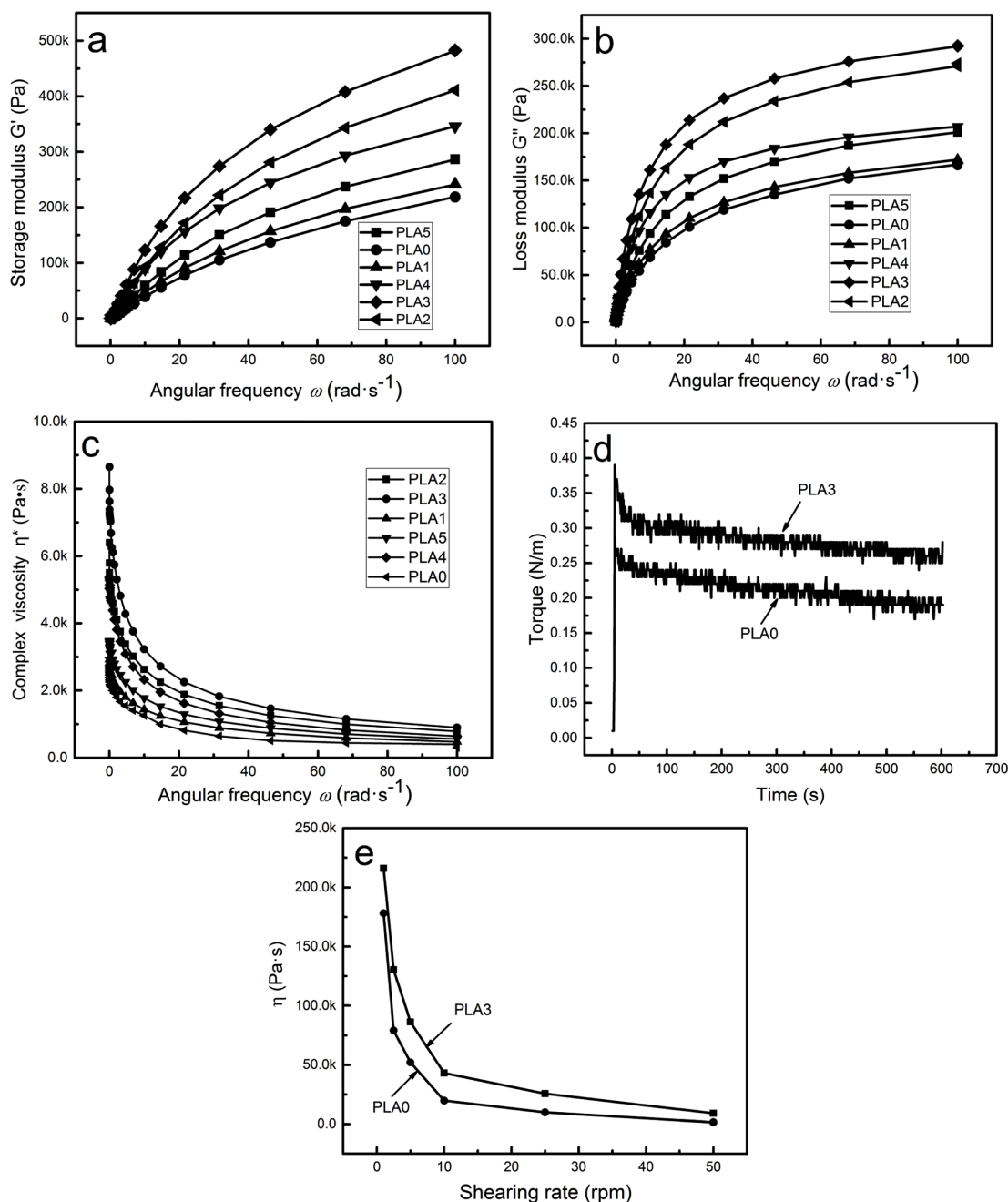


Figure 13. Rheological behavior of PLA and PLA nanocomposites: (a) rotational rheological behavior of storage modulus; (b) rotational rheological behavior of loss modulus; (c) rotational rheological behavior of complex viscosity; (d) capillary rheological behavior of the torque; (e) capillary rheological behavior of apparent viscosity.

PLA5 energy storage modulus (G') and energy loss modulus (G'') change with angular frequency (ω), respectively. According to the diagram, all samples exhibited typical linear rheological behavior, and their G' and G'' increased with the increase of ω , and the G' values were greater than G'' values, indicating that the elasticity of the composite system was stronger than that of the viscosity. When the value of ω was low, the molecular chain of the composites had enough time to remove the entanglement, resulting in low values of G' and G'' . When the ω continued to increase, the relaxation time of the molecular chain was far greater than the deformation time of the system. Therefore, the relaxation of molecular chain could not keep up with the change of external force, the material exhibited elastic behavior. Thereby, the values of G' and G'' both increased. Besides, when the value of ω was high, the value of G' and G'' tended to be stable. This could be explained by the fact, with the increase of ω , the phenomenon of shear thinning occurred, and the influence of ω on the G' and G'' values of the system became smaller.⁴⁹

Figure 13(c) showed the PLA melt was a Newton fluid in the low frequency region, while in the high frequency region it was a non-Newton fluid, showing behavior of shear thinning. Compared with pure PLA, the blends had higher complex viscosity (η^*), this might be due to a strong mutual entanglement between molecular chains of PLA and GO-PMMA. Besides, the blends exhibited more pronounced shear thinning properties, showing the flow characteristics of pseudo plastic fluids.⁵⁰

Furthermore, it could be seen from Figure 13 that after adding GO-PMMA, the G' , G'' , and η^* value of PLA increased, which was due to the reaction between GO-PMMA epoxy group and hydroxyl group in PLA, which enhanced the intermolecular interaction force.⁵¹ In addition, the entanglement of GO-PMMA molecules with PLA chains, the flow resistance increased, so the value of G' , G'' , and η^* increase accordingly. However, when the amount of GO-PMMA was more than 0.3%, the value of G' and G'' decreased slightly, but still higher than that of PLA0. This is consistent with the previous analysis of mechanical properties.

Figure 13(d) and Figure 13(e) shows the capillary rheological analysis for PLA and PLA3. It could be seen from Figure 13(d) that during the feeding process, the torque increased sharply in a short time, then decreased and gradually stabilized. This could explain by the fact that the resistance in the mixing chamber increased gradually, so the torque suddenly increased during the beginning of the feeding process. Sub-

sequently, the material was compacted and crushed under the action of the rotor as it began to melt. With the continuous melting of materials, the resistance was gradually reduced, resulting in the gradual reduction of torque. And the value of torque for the PLA3 was significantly better than that of PLA. This was due to the fact that the formation of hydrogen bonds between GO-PMMA and PLA led to an increase in intermolecular forces, resulting in a decrease in the flow ability of the PLA3 and an increase in torque.⁵² Besides, it was evident from Figure 13(e) that with an increase of shearing rate at constant temperature, the decreasing trend of apparent viscosity (η) of PLA and PLA3 was basically the same. With the addition of optimum amounts of GO-PMMA, the η of PLA and PLA3 gradually decreased. Moreover, the η of the PLA3 was higher than that of PLA. This was due to the fact that the long and flexible macromolecular chains of the PLA/GO-PMMA nanocomposites could entangle with each other, which led to a decrease in the liquefaction of the composite material, and the value of η increased.⁵³ The result was consistent with the result shown in Figure 13(d).

Conclusions

A graft compound GO-PMMA based on GO was synthesized by AGET-ATRP reaction. The structure of GO and GO-PMMA were confirmed by FTIR, XRD, XPS, and TEM. Then, GO-PMMA was added to PLA as a nucleating agent by melt blending to improve the comprehensive performance of PLA. The morphology of PLA/GO-PMMA nanocomposites was studied and its mechanical performance, thermal performance, and rheological properties were tested. The mechanical properties of PLA/GO-PMMA nanocomposites were significantly increased compared with pure PLA. Moreover, DSC and POM results indicated that the crystallization properties of PLA/GO-PMMA nanocomposites were improved significantly. Results of rheological testing showed that GO-PMMA increased the elastic toughness of the PLA. To summarize, GO-PMMA could be eventually used as a nucleating agent to modify PLA and provide a large number of heterogeneous nucleation sites to improve the crystallization rate and crystallization properties of PLA.

Acknowledgments: Financial support from Key Laboratory Open Foundation (NO.2016D03010) of Xinjiang Uygur Autonomous Region of China is greatly acknowledged.

References

1. E. F. Craparo, B. Porsio, M. L. Bondi, G. Giammona, and G. Cavallaro, *Polym. Degrad. Stab.*, **119**, 56 (2015).
2. Y. Zhang, Y. Zhao, H. Pan, X. Lang, H. Yang, and H. Zhang, *Polym. Korea*, **40**, 429 (2016).
3. B. Tyler, D. Gullotti, A. Mangraviti, T. Utsuki, and H. Brem, *Adv. Drug Deliver. Rev.*, **107**, 163 (2016).
4. C. Lantano, I. Alfieri, A. Cavazza, C. Corradini, A. Lorenzi, and N. Zucchetto, *Food Chem.*, **165**, 342 (2014).
5. X. Zhu, R. Huang, T. Zhong, and A. Wan, *Polym. Korea*, **39**, 889 (2015).
6. J. Lund and A. L. Shafer, *J. Ind. Text.*, **29**, 191 (2000).
7. G. Bang and S. W. Kim, *J. Ind. Eng. Chem.*, **18**, 1063 (2012).
8. W. Zhen and J. Sun, *Polym. Korea*, **38**, 299 (2014).
9. Z. Ru, Y. Wang, K. Wang, G. Zheng, L. Qian, and C. Shen, *Polym. Bull.*, **70**, 195 (2013).
10. E. Mascheroni, V. Guillard, F. Nalin, L. Mora, and L. Piergiovanni, *J. Food Eng.*, **98**, 294 (2010).
11. A. Abdalhay, K. H. Hussein, L. Casettari, K. A. Khalil, and A. S. Hamdy, *Mater. Sci. Eng., C*, **60**, 143 (2016).
12. N. D. Geyter, R. Morent, T. Desmet, M. Trentesaux, L. Gengembre, and P. Dubruel, *Surf. Coat. Technol.*, **204**, 3272 (2010).
13. H. Xiang, Y. Mu, C. Hu, and X. Luo, *J. Nanomater.*, **2017**, 10 (2017).
14. R. Arjmandi, A. Hassan, S. J. Eichhorn, M. K. M. Haafiz, Z. Zakaria, and F. A. Tanjung, *J. Mater. Sci.*, **50**, 3118 (2015).
15. S. I. Tverdokhlebov, E. N. Bolbasov, E. V. Shesterikov, L. V. Antonova, A. S. Golovkin, and V. G. Matveeva, *Appl. Surf. Sci.*, **329**, 32 (2015).
16. H. S. Han, J. M. You, H. Jeong, and S. Jeon, *J. Nanosci. Nanotechnol.*, **14**, 4050 (2014).
17. Y. Cao, J. Feng, and P. Wu, *Carbon*, **48**, 3834 (2010).
18. Y. H. Cai, Y. Tang, and L. S. Zhao, *J. Appl. Polym. Sci.*, **132**, 1 (2015).
19. Y. Chen, A. Zhang, L. Ding, Y. Liu, and H. Lu, *Composites Part B*, **108**, 386 (2017).
20. X. Yang, N. Zhao, and F. J. Xu, *Nanoscale*, **6**, 6141 (2014).
21. X. Zhan, Y. Yan, Q. Zhang, and F. Chen, *J. Mater. Chem. A*, **2**, 9390 (2014).
22. F. Perreault, M. E. Tousley, and M. Elimelech, *Environ. Sci. Technol. Lett.*, **1**, 71 (2016).
23. B. Kim, J. Jeong, J. H. Jung, B. S. Kim, K. S. Jung, and H. J. Paik, *Polym. Korea*, **38**, 671 (2014).
24. M. Kumar, J. S. Chung, and S. H. Hur, *Nanoscale Res. Lett.*, **9**, 345 (2014).
25. W. S. Hummers and R. E. Offeman, *J. Am. Chem. Soc.*, **80**, 1339 (1958).
26. X. Wu and D. Y. C. Leung, *Appl. Energ.*, **88**, 3615 (2011).
27. J. F. Zhong, X. S. Chai, X. L. Qin, and S. Y. Fu, *Carbohydr. Polym.*, **86**, 367 (2011).
28. X. S. Chai, J. F. Zhong, and H. C. Hu, *J. Chromatogr. A*, **1238**, 128 (2012).
29. S. H. Lee, D. R. Dreyer, J. An, A. Velamakanni, R. D. Piner, and S. Park, *Macromol. Rapid Commun.*, **31**, 281 (2010).
30. K. Qi, Y. Sun, H. Duan, and X. Guo, *Corros. Sci.*, **98**, 500 (2015).
31. T. Kotre, O. Nuyken, and R. Weberskirch, *Macromol. Rapid Commun.*, **23**, 871 (2015).
32. P. Opaprakasit, M. Opaprakasit, and P. Tangboriboonrat, *Appl. Spectrosc.*, **61**, 1352 (2007).
33. G. Gonçalves, P. A. A. P. Marques, A. B. Timmons, I. Bdkin, M. K. Singh, and N. Emami, *J. Mater. Chem.*, **20**, 9927 (2010).
34. L. Xu, B. Yin, H. Yan, A. Ma, and M. Yang, *Rsc. Adv.*, **5**, 82005 (2015).
35. H. Wang and Z. Qiu, *Thermochim. Acta*, **527**, 40 (2012).
36. L. Lin, J. Qiu, and E. Sakai, *Chem. Eng. J.*, **209**, 20 (2012).
37. C. Bao, L. Song, W. Xing, B. Yuan, C. A. Wilkie, and J. Huang, *J. Mater. Chem.*, **22**, 6088 (2012).
38. M. Shayan, H. Azizi, I. Ghasemi, and M. Karrabi, *Carbohydr. Polym.*, **124**, 237 (2015).
39. L. Wang, Y. N. Wang, Z. G. Huang, and Y. X. Weng, *Mater. Des.*, **66**, 7 (2015).
40. T. Lu, S. Liu, M. Jiang, X. Xu, Y. Wang, and Z. Wang, *Composites Part B*, **62**, 191 (2014).
41. B. Chieng, N. Ibrahim, Y. Wan, M. Hussein, Y. Then, and Y. Loo, *Polymers*, **6**, 2232 (2014).
42. M. Jawaid, A. Hassan, and H. Balakrishnan, *J. Compos. Mater.*, **48**, 769 (2014).
43. H. D. Huang, P. G. Ren, J. Z. Xu, L. Xu, G. J. Zhong, and B. S. Hsiao, *J. Membrane Sci.*, **464**, 110 (2014).
44. Z. Xu, Y. Niu, L. Yang, W. Xie, H. Li, and Z. Gan, *Polymer*, **51**, 730 (2010).
45. A. Babanalbandi, D. Hill, D. Hunter, and L. Kettle, *Polym. Int.*, **48**, 980 (2015).
46. J. Henricks, M. Boyum, and W. Zheng, *J. Therm. Anal. Calorim.*, **120**, 1 (2015).
47. Y. Xu, W. Yu, and C. Zhou, *RSC Adv.*, **4**, 55435 (2014).
48. M. K. Fehri, C. Mugoni, P. Cinelli, I. Anguillesi, M. B. Coltelli, and S. Fiori, *Express. Polym. Lett.*, **10**, 274 (2016).
49. R. Salehiyan, A. A. Yussuf, and A. Akbari, *J. Elastom. Plast.*, **47**, 69 (2015).
50. M. J. Carbone, M. Vanhale, B. Goderis, and P. Van Puyvelde, *J. Polym. Eng.*, **35**, 169 (2015).
51. H. Eslami and M. R. Kamal, *J. Appl. Polym. Sci.*, **129**, 2418 (2013).
52. J. J. Cooper-White and M. E. Mackay, *J. Polym. Sci., Part B: Polym. Phys.*, **37**, 1803 (1999).
53. A. Helle, S. Hirsjärvi, L. Peltonen, J. Hirvonen, and S. K. Wiedmer, *J. Chromatogr. A*, **1178**, 248 (2008).